

Microwave, magnetic, and structural properties of nanocrystalline exchange-coupled Ni₁₁Co₁₁Fe₆₆Zr₇B₄Cu₁ films for high frequency applications

S. D. Yoon,^{1,a)} A. K. Baraskar,^{1,2} A. Geiler,^{1,2} A. Yang,^{1,2} C. Pettiford,^{1,2} N. X. Sun,^{1,2} R. Goswami,³ M. A. Willard,³ C. Vittoria,^{1,2} and V. G. Harris^{1,2}

¹Center for Microwave Magnetic Materials and Integrated Circuits, Northeastern University, Boston, Massachusetts 02115, USA

²Department of Electrical and Computer Engineering, Northeastern University, Boston, Massachusetts 02115, USA

³Naval Research Laboratory, Multifunctional Materials Branch, Washington, 20375, USA

(Received 26 June 2007; accepted 24 January 2008; published online 31 March 2008)

Nanocrystalline structured films of the alloy Ni₁₁Co₁₁Fe₆₆Zr₇B₄Cu₁ were deposited by pulsed laser ablation deposition onto fused quartz substrates. A substrate temperature of 300 °C was found to produce films consisting of body-centered-cubic (bcc) metallic grains suspended in an amorphous matrix. The bcc grain size ranged from 5–8 nm for substrate temperatures up to 300 °C. Measured values of coercivity were consistently below 4 Oe for films having a saturation magnetization, as $4\pi M_s$, of ~16 kG with in-plane uniaxial anisotropy fields of 25 to 30 Oe. The ferromagnetic resonance peak-to-peak derivative linewidth was measured to be 34 Oe at a frequency of 9.61 GHz. The zero magnetic field ferromagnetic resonance occurred at ~2 GHz. These films exhibit soft magnetic properties, high saturation induction, low microwave loss, and the structural stability desirable for thin film inductor applications. © 2008 American Institute of Physics.

[DOI: 10.1063/1.2899094]

INTRODUCTION

With the increasing demand for smaller passive components that operate at higher frequencies and temperatures, the electronics industry is in need of improved alloys for use as thin film inductors. Specifically, these materials should possess a high permeability, high saturation magnetization, and low coercivity. Ideally, they should also have small eddy current losses at the targeted operational frequencies. To this end, we have prepared and studied the dc and high frequency magnetic properties of nanocrystalline exchange-coupled alloy films. The alloys we have chosen have attractive properties when prepared as bulk ribbon¹ exhibiting a nanograined microstructure in which metallic crystallites were imbedded within an amorphous matrix. Studies have shown the ribbon materials to have low coercivity, low core losses, low magnetostriction, moderate saturation magnetization, and high permeability.^{1,2} In previous work,³ we have presented the structural and magnetic properties of Ni₅₉Co₂₂Fe₇Zr₇B₄Cu₁ and Ni₆₀Co₂₂Fe₇Zr₇B₄ films with saturation magnetization of $4\pi M_s \sim 7000$ G. In this paper, we present the structure, magnetic, and microwave properties of Ni₁₁Co₁₁Fe₆₆Zr₇B₄Cu₁ alloy films. The present alloy contains more iron (Fe) resulting in films with a saturation magnetization of approximately 16 000 G.

Nanocrystalline soft magnetic materials of this type were first developed by Yoshizawa *et al.* at Hitachi Metals, Ltd.² The first of these alloys had the composition Fe_{73.5}Si_{13.5}Nb₃B₉Cu₁ which today goes by the trade name Finemet™. Herzer⁴ observed a power law relationship be-

tween the coercivity (H_c) and the grain size (D) of nanostructured soft magnetic alloys and subsequently proposed a random anisotropy model that explains the soft magnetic properties. This model is widely accepted today to accurately describe most nanocrystalline exchanged-coupled bulk alloys using a $H_c \propto D^6$ power law relationship. In 1998, Suzuki *et al.*⁵ demonstrated that for systems that possess a strong uniaxial anisotropy, i.e., much greater than the random nanocrystalline anisotropy, the D^6 law did not hold but instead a D^3 correspondence was found for three-dimensional nanostructured materials. We have found that for films having a well-defined uniaxial anisotropy, a power law relationship is observed with $H_c \propto \sim D^3$.⁶ In that earlier study, we found the best soft magnetic results were obtained from films deposited at $T_S=300$ °C. In this study, we present results of the optimal growth conditions for films of Ni₁₁Co₁₁Fe₆₆Zr₇B₄Cu₁. Since this alloy has substantially higher magnetization, it offers greater potential for applications as an inductor material.

EXPERIMENTAL

In the present study, thin film processing involved the laser ablation of a pressed powder alloy compact of composition Ni₁₁Co₁₁Fe₆₆Zr₇B₄Cu₁. The constituent elements were 99.9% pure. Films, ranging in thickness from 200–300 nm, were deposited onto fused quartz substrates. Deposition of these films was carried out at a constant laser energy of 400 mJ ($\lambda=248$ nm) and at 10 mTorr of argon gas pressure. Prior to establishing a dynamic vacuum of argon, the chamber was evacuated to less than 1×10^{-6} Torr. The substrate temperature (T_S) was varied from ambient to 600 °C. The

^{a)}Electronic mail: syoon@ece.neu.edu.

deposition rate was determined by the laser pulse rate. In order to improve film adhesion to the substrate, a repetition rate of 1 Hz was used in the first 10 min followed by 10 Hz for the next 60 min.

Structural properties were determined by x-ray diffraction (XRD) and transmission electron microscopy (TEM). Lattice parameters of the nanocrystalline phase were deduced from XRD patterns using standard practices with grain size determined by Scherrer analysis.⁷ All XRD spectra were obtained using a Phillips X'pert Pro instrument with a Cu $K\alpha$ source ($\lambda = 1.5406 \text{ \AA}$). Images of the film nanostructure and microstructure were obtained by traditional TEM. All TEM measurements were performed on a JEOL 2010 instrument operating at 200 keV. TEM samples were prepared from the thin film samples in a Fischione ion mill at a gun voltage of 5 kV, a current of 4 mA, and an incident angle of 12° .

Magnetic properties such as coercivity, anisotropy field, and remanent and saturation magnetizations (as $4\pi M_S$) were measured from hysteresis loops collected using a vibrating sample magnetometer (VSM) with the applied magnetic field aligned along both the in-plane easy and hard magnetic axes. Magnetization versus temperature (T) was performed on selected films under an external dc magnetic field of 200 Oe using a Quantum Design physical properties measurement system (PPMS) and a VSM for low and high temperatures, respectively. Ferromagnetic resonance (FMR) of the films was measured using a cavity technique operating in the TE_{102} mode. Room temperature FMR spectra were taken at an X-band frequency ($f = 9.61 \text{ GHz}$) using a differential power absorption technique operating with a Varian microwave bridge as the microwave source and a Varian E-line console which employed a built in lock-in amplifier and a 100 kHz modulation signal for detection of the absorption signal. Broadband FMR measurements were performed using a technique based on a planar device consisting of a junction formed by conjoining a shorted slotline and coplanar waveguide. Propagation of the microwave signal is channeled through the sample placed over the junction.⁸ A low frequency magnetic field modulation with a lock-in detection scheme was used to improve signal sensitivity. This slotline microwave device allows the measurement of FMR from 0.01 to 20 GHz and from 26 to 40 GHz due to the availability of microwave sweepers. A standard collinear four point probe technique was used to measure the dc electrical resistivity (ρ) at room temperature for all films.

RESULTS AND DISCUSSIONS

θ - 2θ XRD patterns of the films deposited at different substrate temperatures are shown in Fig. 1. The Miller indices of all detected diffraction peaks are denoted on the data corresponding to the sample grown at the highest substrate temperature.^{6,7} All the diffraction features can be correlated to either the body-centered-cubic (bcc) or the face-centered-cubic (fcc) phases. These appear depending upon the T_S . Film samples deposited at $T_S \leq 400^\circ \text{C}$ showed XRD peaks indexed to only the bcc phase. In contrast, the bcc phase was measured to coexist with an fcc phase in films deposited at $T_S \geq 400^\circ \text{C}$. The bcc phase is identified by the appearance

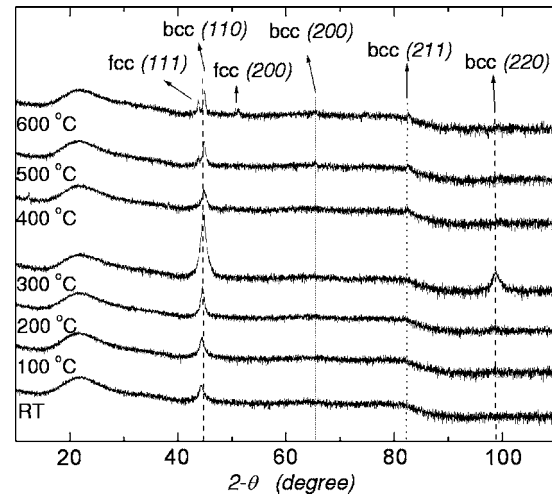


FIG. 1. XRD spectra collected using Cu $K\alpha$ radiation, vertically offset to allow comparison. The Miller indices of all diffraction features are indexed to bcc and fcc phases for the film grown at the highest substrate temperature.

of the (110) peak centered at 2θ values from 44.21° to 44.85° , and the (220) peak centered near 98° .⁷ The relationship between lattice parameters and T_S is shown in Fig. 2. The lattice parameters for the bcc phase range from 0.288 ± 0.001 to $0.286 \pm 0.001 \text{ nm}$ as the T_S is increased to 600°C . This can be attributed largely to the changing composition of the crystallite phase with increasing T_S , although the role of residual stress in the film cannot be ignored. The bcc lattice parameters with various T_S are compared to the lattice parameters measured by Willard *et al.* for bulk $\text{Ni}_{10.7}\text{Co}_{10.7}\text{Fe}_{64.1}\text{Zr}_{8.5}\text{B}_5\text{Cu}_1$.¹ The bulk samples were prepared as amorphous ribbons by the melt spinning technique and then annealed at 500°C for 1 h to obtain the optimum nanostructure. The bcc phase lattice parameter was measured to be 0.288 nm , which is similar to the lattice parameter of the pulsed laser deposition (PLD) film (0.288 nm) deposited at $T_S = 100\text{--}200^\circ \text{C}$. As the T_S is increased, the film bcc lattice parameter decreases to a value of $0.287 \pm 0.001 \text{ nm}$, nearly equivalent to that of bcc iron. We speculate that this reduction in the lattice parameter results from the expulsion

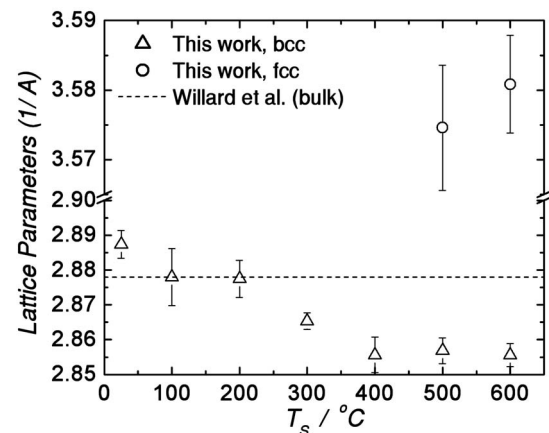


FIG. 2. Lattice parameters of the samples for bcc (Δ) and fcc (\circ) phases vs the substrate temperature (T_S).

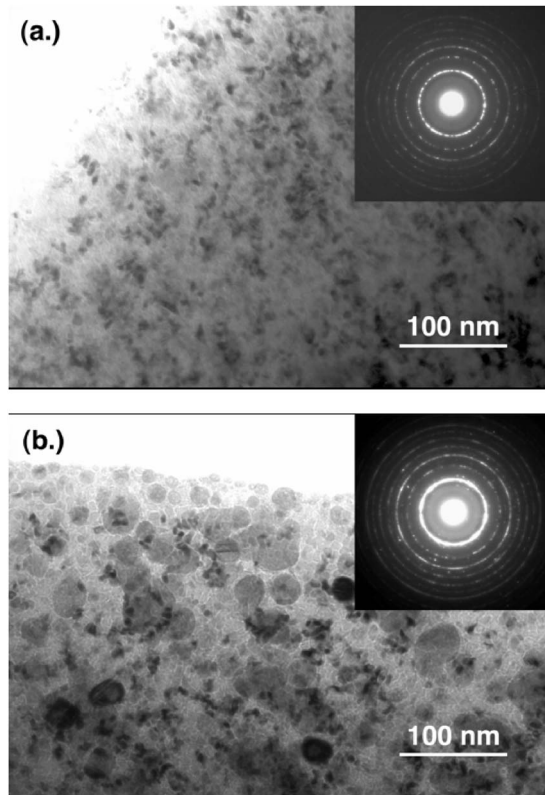


FIG. 3. TEM image of the samples grown at (a) $T_S=300$ °C and (b) $T_S=400$ °C. Selected area diffractions patterns are provided as insets to each panel.

of the non-Fe constituent elements from the bcc phase as the T_S is increased and as the fcc phase rich in Ni and Co forms.

Conventional TEM images for the film deposited at $T_S=300$ and 400 °C are shown in Fig. 3. Grains of around 5–8 nm in diameter surrounded by an amorphous matrix (white) that is ~ 1 nm in thickness were measured from Fig. 3(a) where T_S was 300 °C. A TEM image is shown in Fig. 3(b), for the film deposited at $T_S=400$ °C, depicting a bimodal distribution in grain size with bcc grains of 5–7 nm in diameter coexisting with larger fcc grains of 25–30 nm diameter and an amorphous matrix.

A comparison of the structural and magnetic properties of the films was performed to determine the optimal thin film nanostructure. Figure 4 shows the average grain size versus T_S and demonstrates clearly temperatures (T) dependence. The average grain size (D) was consistently less than 9 nm for samples having $T_S < 400$ °C. Increased grain growth occurs in films deposited at higher T_S with D greater than 60 nm for samples grown at T_S greater than 500 °C. Previous TEM results³ of ribbon samples indicate that the volume of the amorphous phase, rich in Zr and B, is reduced as the annealing temperature is increased. The amorphous phase regions were reduced from 2 to 3 nm at $T_S=200$ °C to ~ 1 nm size for 300 °C. We postulate, as T_S increased to 300 °C the volume fraction of the crystallites increased at the expense of the amorphous phase. However, at $T_S > 400$ °C crystallites quickly grew presumably via an Oswald ripening mechanism to >60 nm size. In this case, the

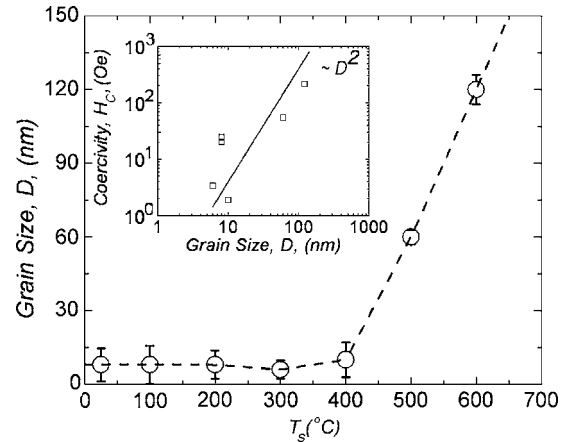


FIG. 4. Grain size (D) vs T_S . The inset figure illustrates the power law dependence between coercivity (H_c) and D .

volume of the crystallites relative to the amorphous phase remained nearly constant but the crystallites grew in size at the expense of the bcc phase.

Hysteresis loops obtained with applied magnetic fields aligned along the magnetic easy and hard axes (in-plane) were collected for all films. The in-plane easy and hard directions were defined by measuring the remanence magnetization with an angular variation of the applied in-plane field. The origin of an in-plane anisotropy is not discussed here but may result from a chemical pair order anisotropy that is not unexpected for these alloys. From these data, coercivity, uniaxial anisotropy field, and remanent and saturation magnetization values were measured. Figure 5(a) shows the hysteresis loops for the film grown at $T_S=300$ °C. Coercivity was measured to be 1.9 and 3.4 Oe for films deposited at $T_S=300$ and 400 °C, respectively. H_c values increased dramatically, $H_c > 50$ Oe, for the films deposited at $T_S > 400$ °C. The inset to Fig. 4 is a plot of coercivity H_c versus D for $\text{Ni}_{11}\text{Co}_{11}\text{Fe}_{66}\text{Zr}_8\text{B}_4\text{Cu}_1$ alloy films. A power law dependence is clearly demonstrated. Typical power law relationships between the coercivity and the grain size have been reported in ribbon materials to be six when the ribbons have little induced anisotropy or three when a long range uniaxial anisotropy is present (as found in field annealed samples).^{4,5}

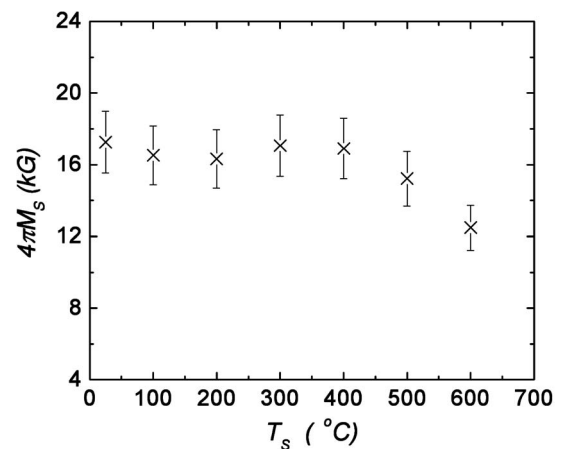


FIG. 5. Saturation magnetization ($4\pi M_s$) vs T_S measured by VSM hysteresis loops.

In both of these instances, exchange correlation length (L_{ex}) was determined to be much larger than the grain size but much smaller than the sample dimension. For our samples, the restricted thickness of the thin film geometry (200–300 nm) becomes an important factor when considering the power law relationship. The exchange correlation for our films were estimated to be 80–100 nm in length using either ripple theory or two-dimensional random anisotropy models.^{9,10} Measured values of saturation magnetization (1.6 T), grain size ($D=8$ nm), film thickness (250 nm), and anisotropy field (~ 50 Oe) were used in these calculations. Estimations of the exchange stiffness ($A \sim 10^{-11}$ J/m) and magnetocrystalline anisotropy of the crystalline phase ($K_1 \sim 10^4$ J/m³) were assumed due to the Fe-rich composition of the sample. The further assumption that the coercivity of the film (2 Oe) was similar to the field at which domain walls can move through the material resulted in the exchange length value of 80 nm (see Ref. 10 for calculation details). Using the two-dimensional random anisotropy model the estimated L_{ex} was found to be about 100 nm [using $L_{\text{ex}} = (A/\langle K \rangle)^{1/2}$ and $\langle K \rangle \sim K_1^2 D^2/A$, see Ref. 9]. In either case, the exchange length is a large fraction of the total thickness of the film and the resulting power law of two is predicted using either model.

The magnetization for films deposited at $T_S < 400$ °C remains constant near 16 kG within the uncertainty of the measurement but decreases at higher T_S . This reduction in magnetization is likely due in part to the formation of a surface oxide occurring at higher T_S . Another source of reduced magnetization may be the formation of a paramagnetic fcc phase. Evidence for the fcc phase appears in the selected area diffraction spectra of samples grown at temperatures ≥ 500 °C. (see Fig. 3). Figure 5 shows the trend for the reduction of $4\pi M_S$ as related to T_S . The temperature dependence of saturation magnetization, with applied field of $H = 200$ Oe, was measured for the film deposited at $T_S = 300$ °C, see Fig. 6(b). The measurement was performed using both a PPMS at temperature below room temperature and a VSM for temperatures than room temperature. Saturation magnetization ($4\pi M_S$) was constant at ~ 16 kG up to 460 K, and then decreased as temperature was increased. Curie temperature was estimated to be near 720 K from mean field fits to the data; although the sample likely is partially changing to a paramagnetic fcc phase at the highest temperatures (similar to the high T_S samples). For fitting the data, mean field theory $4\pi M(T) \sim 4\pi M_0(T - T_c)^\beta$, was examined with $\beta \sim 0.35 - 0.5$, where $4\pi M_0$ is saturation magnetization at $T = 0$ K. A good fit is obtained with a T_c of 1000 K. This relatively high value of T_c may be due to surface oxidation. The data appearing below 30 K may reflect a spin glass effect.

FMR measurements were performed to determine the microwave properties of the films. First, measurements were carried out using an X-band microwave bridge with an X-band cavity. The FMR linewidths (ΔH) were measured at $f = 9.61$ GHz for the films deposited at $T_S =$ ambient to 600 °C. FMR ΔH versus T_S data are presented in Fig. 7(a). Values are strongly correlated with H_c and D indicating that smaller values of D give rise to lower magnetic rf loss. The

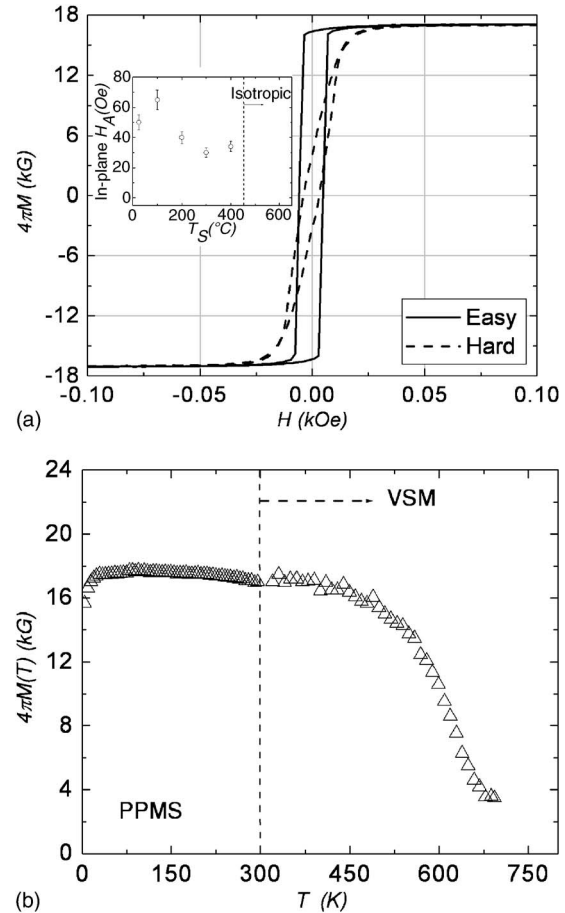
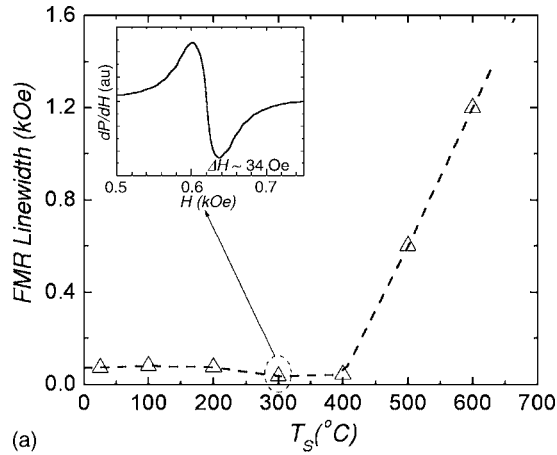
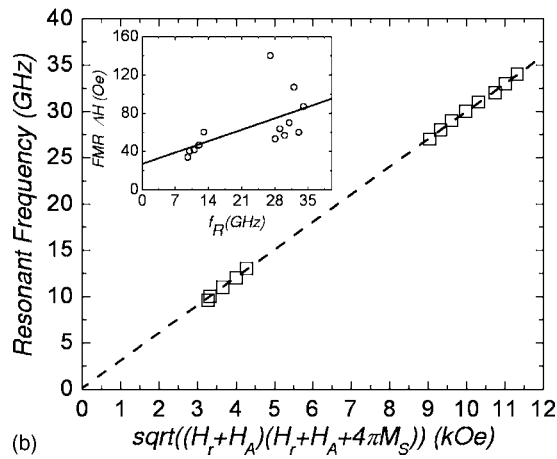


FIG. 6. (a) Hysteresis loops for the film samples grown at $T_S = 300$ °C. Data were collected with the applied magnetic field aligned along the in-plane easy (solid line) and hard axes (dashed line). An uniaxial anisotropy field (H_A) of ~ 30 Oe was measured at the saturation point of the dashed line. Inset plot shows uniaxial anisotropy fields vs T_S . (b) Temperature dependence of $4\pi M_S$ for the film deposited at $T_S = 300$ °C.

analysis of these results follows that proposed in Refs. 11 and 12. When considering this relationship, there are two distinct regimes: (i) the independent particle regime, which coincides with large grains (LG), and (ii) the exchange-narrowed regime, which corresponds to small grains (SG). For the purposes of this study, we define the SG regime to extend from $T_S \leq 300$ °C in which D is typically below 10 nm and the LG regime from $T_S > 400$ °C in which D is typically above 20 nm. As described for the LG regime, the FMR linewidth broadening is caused by the random distribution of local anisotropy fields, which add to or subtract from, the applied field. Even though the FMR condition described in Refs. 11 and 12 (out-of-plane FMR) is not the same as the one used here (in-plane FMR measurement), our FMR measurements show a similar relationship between the magnetic anisotropy field H_A and ΔH . We have measured the in-plane hard H_A value to range from 30 to 50 Oe in films deposited with $T_S \leq 400$ °C. However, the in-plane magnetization becomes isotropic for films deposited at $T_S > 400$ °C. The FMR linewidth shows a strong dependency upon grain size and local uniaxial anisotropy. While the grain size increases with increases T_S , the local in-plane anisotropy was destroyed as the grain size grew beyond 10 nm. The linewidth distribution in the LG regime is given by the formula¹¹



(a)



(b)

FIG. 7. (a) FMR derivative linewidths (ΔH) vs T_S measured at X-band (9.6 GHz) frequency. Inset plot shows FMR spectrum with $\Delta H \sim 34$ Oe measured for the film grown at $T_S = 300$ °C. (b) FMR resonant frequency (f_R) vs resonant field relation obtained from the film with $T_S = 300$ °C. Inset shows FMR ΔH vs f_R .

$$\Delta H^{\text{LG}} \sim (5/3)H_A, \quad (1)$$

where $H_A = 2K/M = 30$ Oe from the VSM hysteresis data of the film deposited at $T_S = 300$ °C. The estimated FMR linewidth can be obtained by using Eq. (1) which provides a $\Delta H \sim 42$ Oe, a value that is quite similar to the experimental values obtained in this study; the lowest ΔH was measured to be 34 Oe for the film deposited at $T_S = 300$ °C, see Fig. 7(a).

We also have measured the broadband FMR properties of these film samples by using a rf resonating device constructed by conjoining a coplanar wave guide and a slot line. Using this device we have measured the FMR in the film deposited at 300 °C over a frequency range between 10 and 34 GHz. In general, the FMR resonant frequency relation with an applied magnetic field can be obtained from the FMR condition which is presented as Eq. (2) and in Fig. 7(b).

The FMR condition for the film geometry is

$$\frac{\omega}{\gamma} = \sqrt{(H_r + H_A)(H_r + H_A + 4\pi M_S)}, \quad (2)$$

where H_r is the dc applied field and H_A is the uniaxial anisotropy field. The gyromagnetic splitting factor is

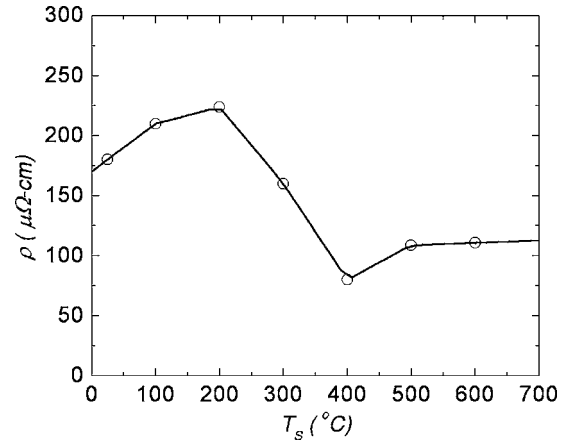


FIG. 8. dc electrical resistivity (ρ) of films vs T_S measured using a standard four point collinear probe technique at room temperature. The line connects the data points and is intended as a guide to the eye.

$$\gamma = \frac{ge}{2mc}, \quad (3)$$

where e , m , and c are electron charge, electron mass, and the speed of light, respectively. We deduce a g factor of 2.13 from the FMR data assigning $4\pi M_S = 16$ kG and $H_A = 25$ Oe (obtained from VSM data) from the slope shown in Fig. 7(b). In Ref. 3, a g value of 2.21 was deduced for $\text{Ni}_{58.96}\text{Co}_{22}\text{Fe}_{7.04}\text{Zr}_7\text{B}_4\text{Cu}_1$ alloy films. The relatively high value reported in Ref. 3 was attributed to the higher concentrations of Ni and Co while the g value of 2.13 provided here is appropriate for the Fe-rich composition. From Eq. (2), the zero field FMR appears near 2 GHz. Therefore, this film may be suitable as a low loss inductor material for operational frequencies up to 2 GHz. The current broadband FMR measurement system does not allow for measurement below 10 GHz due to the lack of a rf sweep oscillator operating below 10 GHz. Therefore, we could not explore the sample performance in this frequency range.

Room temperature dc resistivity for all films of $\text{Ni}_{11}\text{Co}_{11}\text{Fe}_{66}\text{Zr}_8\text{B}_4\text{Cu}_1$ was measured by a standard four point probe technique. The films showed moderate resistivity values ranging from 100–225 $\mu\Omega$ cm at room temperature due principally to the large volume of the amorphous matrix. The resistivity increased linearly with T_S reaching a maximum of 225 $\mu\Omega$ cm for the 200 °C sample with the added resistivity likely due to scattering from the copious grain boundaries and the glassy intergranular amorphous phase. The resistivity decreased for the samples grown >200 °C which we attribute to the large volume fraction of the crystalline phase (see Figs. 3 and 8). The highest values favorably compare with the best Metglas™ alloys and reflect the reduced eddy current losses in these films. For the best Metglas™ alloys, the highest resistivity was measured to be ~ 180 $\mu\Omega$ cm, which is 25% lower than the value for our best PLD films ($T_S = 200$ °C).^{13,14}

CONCLUSIONS

Structural, magnetic, and microwave properties of nanocrystalline films of $\text{Ni}_{11}\text{Co}_{11}\text{Fe}_{66}\text{Zr}_8\text{B}_4\text{Cu}_1$ alloy are reported. The films were grown on quartz substrates using PLD from

homogeneous targets of the above composition at substrate temperatures ranging from ambient to 600 °C. The optimal growth temperature for PLD processing was found to be 300 °C at 10 mTorr argon gas pressure. The films contain two distinct phases with bcc metallic grains suspended in an amorphous matrix. The softest magnetic films were deposited at 300 °C and had coercivity values of 3.4 Oe with a saturation magnetization $4\pi M_s$ of $\sim 16\,000$ G. Films grown at substrate temperatures below 400 °C had bcc grains of 5–8 nm in diameter separated by an amorphous phase of thickness ~ 1 nm. The relationship between grain size and coercivity followed a power law dependence with $H_c \propto \sim D^2$. FMR linewidths of 30–50 Oe at 9.6 GHz and a maximum dc electrical resistivity of $225 \times 10^{-6} \Omega \text{ cm}$ indicate that these films may be suitable for applications as planar inductors up to its zero field FMR frequency of 2 GHz.

¹M. A. Willard, J. C. Claassen, R. M. Stroud, T. L. Francavilla, and V. G. Harris, *IEEE Trans. Magn.* **38**, 3045 (2002).

²Y. Yoshizawa, S. Oguma, and K. Yamauchi, *J. Appl. Phys.* **64**, 6044

(1998).

³S. Joshi, S. D. Yoon, A. Yang, N. X. Sun, C. Vittoria, V. G. Harris, R. Goswami, M. Willard, and N. Shi, *J. Appl. Phys.* **99**, 08F115 (2006).

⁴G. Herzer, *IEEE Trans. Magn.* **26**, 1397 (1990).

⁵K. Suzuki, G. Herzer, and J. M. Cadogan, *J. Magn. Magn. Mater.* **177–181**, 949 (1998).

⁶A. K. Baraskar, S. D. Yoon, A. Geiler, A. Yang, C. N. Chinasami, Y. Chen, N. Sun, C. Vittoria, R. Goswami, M. Willard, and V. G. Harris, *J. Appl. Phys.* **101**, 09M519 (2007).

⁷B. D. Cullity, *Elements of X-ray Diffraction*, 2nd ed. (Addison-Wesley, Reading, 1978), p. 102.

⁸S. Zhang, S. A. Oliver, N. E. Israeloff, A. Widom, and C. Vittoria, *J. Appl. Phys.* **81**, 4307 (1997).

⁹K. Suzuki, J. M. Cadogan, V. Sahajwalla, A. Inoue, and T. Masumoto, *J. Appl. Phys.* **79**, 5149 (1996).

¹⁰H. Hoffmann and T. Fujii, *J. Magn. Magn. Mater.* **128**, 395 (1993).

¹¹M. Rubinstein, V. G. Harris, and P. Lubitz, *J. Magn. Magn. Mater.* **234**, 306 (2001).

¹²E. Schlomann and J. R. Zeender, *J. Appl. Phys.* **29**, 341 (1958).

¹³F. E. Luborsky, *Amorphous Ferromagnets*, edited by E. P. Wohlfarth (North-Holland, Amsterdam, 1980), Vol. 1, pp. 474.

¹⁴R. C. O'Handley, R. Hasegawa, R. Ray, and C.-P. Chou, *Appl. Phys. Lett.* **29**, 330 (1976).